



Observations of Temporal Variations in the 5303 Å Emission Line During a Coronal Mass Ejection Without Any Associated Solar Flare

V. Muthu Priyal , R. Ramesh , Jagdev Singh , and K. Sasikumar Raja

Indian Institute of Astrophysics, Koramangala 2nd Block, Bangalore 560034, Karnataka, India

Received 2024 December 22; revised 2025 March 6; accepted 2025 March 7; published 2025 April 17

Abstract

Reports using total solar eclipse data indicate that the 5303 Å emission line is a promising tool for observing the thermodynamic changes due to coronal mass ejections (CMEs) close to the Sun. The Visible Emission Line Coronagraph (VELC) on board ADITYA-L1, the recently launched first Indian space solar mission, has now provided an opportunity to regularly observe the solar corona in the 5303 Å emission line. We present the first long-duration temporal observations of activity associated with a flareless CME from an active region at the west limb of the Sun, with the VELC. The observations were in the sit-and-stare mode for ≈ 7 hr. Our analysis shows a steady increase in the intensity of the line by $\approx 57\%$, followed by a gradual decrease to the initial level. The width of the line also showed changes, but opposite to that in the intensity. The width slowly decreased from 0.97 ± 0.01 Å to 0.87 ± 0.01 Å and then increased back. The change is $\approx 10\%$. The effective temperatures corresponding to each of the above two widths are $3.39 \pm 0.1 \times 10^6$ K and $2.74 \pm 0.1 \times 10^6$ K, respectively. The Doppler velocity changed gradually from 0 ± 0.5 km s $^{-1}$ to -3 ± 0.5 km s $^{-1}$ during the abovementioned intensity increase phase. It slowly reverted to 0 ± 0.5 km s $^{-1}$ when the intensity decreased.

Unified Astronomy Thesaurus concepts: [The Sun \(1693\)](#); [Solar corona \(1483\)](#); [Solar coronal mass ejections \(310\)](#); [Solar activity \(1475\)](#); [Solar coronal lines \(2038\)](#)

1. Introduction

Analysis of the spectral profiles of the emission lines is one of the important techniques to study the physical conditions in the solar atmosphere. The spectroscopic observations provide unique information on the width and Doppler shift of the emission in addition to the intensity of the line. The imaging observations will generally have some contribution from the continuum wavelengths depending on the passband of the filter used, in addition to emission flux. While the line widths are useful to verify and constrain the coronal heating theories, the Doppler shifts help to infer the plasma motions along the line-of-sight (LoS) direction to the observer. It is well known that spectroscopic as well as narrowband imaging observations in the 5303 Å coronal emission line (green line) are a useful tracer of solar activity (see, e.g., M. Rybanský et al. 1994a, 1994b; R. C. Altrock 2011; S. R. Habbal et al. 2010, 2021; A. Ding & S. R. Habbal 2017; S. Koutchmy et al. 2019; B. Boe et al. 2022, 2023; G. D. Muro et al. 2023). The historical observations of the line are reported in C. A. Young (1872) and B. Lyot (1932). The emissivity is due to a forbidden transition of the Fe XIV ion at 5303 Å and its maximum near $\approx 1.8 \times 10^6$ K. Observations of the solar corona in the above spectral line have been reported by several authors (see, e.g., R. Ramesh et al. 2024; Y. Zhu et al. 2024 and the references therein). The FWHM of the line computed from the observations is always found to be broader than the thermal width arising from the kinetic temperature of the ions (T_i). The excess is called the nonthermal width or nonthermal velocity (in terms of velocity) and is widely attributed to magneto-hydrodynamic turbulence, propagation of Alfvénic waves, and

reconnections. There are several studies on the intensity and width of the 5303 Å line as a function of the height above the solar limb in the literature (T. Tsubaki 1975; H. Hara & K. Ichimoto 1999; J. Singh et al. 1999, 2004, 2006; I. S. Kim 2000; L. Contesse et al. 2004; M. Mierla et al. 2008; G. D. Muro et al. 2023; Y. Zhu et al. 2024). These observations focused primarily on the spatial variations in the abovementioned spectral parameters, rather than temporal changes in them over a longer period at any given coronal location. Continuous measurements of the line intensity for several hours at a particular height have been reported by S. P. Plunkett et al. (1997), K. Hori et al. (2005), and I. Suzuki et al. (2006) using imaging data in the green line. Similar publications of combined results on the temporal changes in the intensity, width, and Doppler velocity of the line, which require spectroscopic observations for a long duration, are however limited (Y. Zhu et al. 2024 and the references therein). An understanding of the variations in these parameters, particularly during a coronal mass ejection (CME), is important since it would help to understand the dynamic changes near the source region of the CME. We present the first comprehensive measurements of the abovementioned spectral parameters (i.e., intensity, width, and Doppler velocity) from recent spectroscopic observations of the near-Sun phase of a CME in the 5303 Å emission line with Visible Emission Line Coronagraph (VELC). Interestingly, the CME was not accompanied by any flare.

2. Observations and Data Analysis

The VELC payload on board ADITYA-L1 is an internally occulted solar coronagraph with the capability to carry out simultaneous imaging (5000 Å) and spectroscopy (5303, 7892, and 10747 Å) observations from close to the limb. The radius of the occulter is $1.05 R_\odot$. The 10747 Å facility can be operated

Table 1

Parameters of the ADITYA-L1/VELC 5303 Å Emission Line Observations on 2024 July 5

Parameter	Specifications
Spectral dispersion	28.4 mÅ per pixel
FWHM of the narrowband filter	6.5 Å
Location of the center of fourth slit	$r = 1.08 R_{\odot}$ at west limb ($\theta = 270^{\circ}$)
Spatial binning	2 pixels
Spectral binning	1 pixel
Exposure time	5 s for each spectrum
Cadence	61 s
Observation duration	7 hr (12:00–19:00 UT)

either in spectroscopy or spectropolarimetry mode. The field of view (FoV) for the imaging and spectral channels are $1.05\text{--}3.0 R_{\odot}$ and $1.05\text{--}1.5 R_{\odot}$, respectively. The plate scale values are $2''.25$ per pixel (imaging channel), $1''.25$ per pixel (5303 \AA and 7892 \AA spectral channels), and $4''.33$ per pixel (10747 \AA spectral channel.) The size of each pixel is $6.5 \mu\text{m}^2$ for the imaging, 5303 \AA , and 7892 \AA channels. For the 10747 \AA channel, it is $25 \mu\text{m}^2$. The dispersion in the spectroscopy channels is 28.4 m\AA per pixel (5303 \AA), 31.3 m\AA per pixel (7892 \AA), and 223 m\AA per pixel (10747 \AA). Observations are carried out using four straight slits simultaneously. The use of multislit helps to reduce the observing time in the spectral channels by a factor of 4, particularly when the above-mentioned entire FoV is observed. The length of each slit is along the north–south direction of the Sun, and the width (dispersion) is along the east–west direction of the Sun. The FoV covered by the slit length is $\pm 1.5 R_{\odot}$. Typically, the first and fourth slits are used to observe the corona above the east and west limbs of the Sun, respectively. The coronal regions above the north and south limbs of the Sun are observed using the second and third slits together. The observations can be carried out in either sit-and-stare mode or raster scan mode (B. R. Prasad et al. 2023; R. Ramesh et al. 2024; J. Singh et al. 2025). The slit width (dispersion direction) is $50 \mu\text{m}$, equivalent to $9''.6$. A linear scan mechanism (LSM) is used to position the coronal light on the slits. The second and third slits are equidistant between the first and fourth slits. The spacing between the adjacent slits is $0.75 R_{\odot}$. A distance range of $0.75 R_{\odot}$ in the east–west direction of the Sun can be scanned (observed) using each slit, by moving the LSM. The total FoV that can be observed in the east–west direction using all four slits together is $\pm 1.5 R_{\odot}$.

The observations were carried out with the 5303 \AA spectroscopy channel on 2024 July 5 from 11:00 UT–19:30 UT in the sit-and-stare mode. Considering the size of the Sun’s image on the day of the observations from the Sun-Earth Lagrangian L1 location and the occulter size in the VELC, we find that the occulter edge will be at $r \approx 1.08 R_{\odot}$ in the corona. The LSM was positioned such that the center of the fourth slit observes the corona at $r = 1.08 R_{\odot}$ to the west of the Sun’s central meridian. The observational parameters related to the present work are listed in Table 1. We used onboard spatial binning of 2 pixels to reduce the data volume. Totally 501 spectra were recorded. Each spectrum was corrected for dark current, curvature of the spectra, flat field, and background as described in J. Singh et al. (2025). Then the observed emission line profile was fitted with a Gaussian to compute the peak intensity, width of the emission line, and Doppler velocity at

each spatial location along the slit (Figure 1). The average wavelength of the emission line from a large number of high spectral resolution observations with the 25 cm Norikura coronagraph is 5302.8 \AA , which corresponds to 5304.3 \AA in vacuum (J. Singh et al. 2004, 2006). This wavelength was used as a reference to compute the Doppler velocity. Note that the corresponding wavelength for the line in vacuum is 5304.771 \AA , as per the CHIANTI atomic database.¹ We briefly explain here the methodology followed by us for photometric calibration and background subtraction. Solar disk images and spectra around emission lines were obtained in-orbit by off-pointing the spacecraft from the Sun center by $16'$, and using a 45 mm diameter neutral density (ND) filter of optical density 4 mounted on a shutter in front of the entrance aperture of VELC whose diameter is 147 mm. The shutter, kept open during the routine coronal observations, was closed during the above-mentioned solar disk light observations. The use of a smaller aperture and the transmission of the ND filter (0.64×10^{-4} at 5303 \AA) decrease the disk light intensity by a factor of $\approx 6 \times 10^{-6}$ making it similar to coronal intensity. Considering the observed count at the disk center in the continuum region of the spectrum and the standard solar flux, we found that one count observed with VELC at 5303 \AA corresponds to $0.0173 \text{ erg s}^{-1} \text{ cm}^{-2} \text{ \AA}^{-1} \text{ sr}^{-1}$. Regarding the background subtraction, the observed coronal spectrum shows absorption lines due to scattered disk light in the instrument. The scattered light and continuum emission of the solar corona contribute to the background in the coronal spectrum. The solar disk spectrum obtained in-orbit is used to remove the background emission by comparing the signals at the continuum region in both the coronal and disk spectrum. The disk count is scaled to the same value as the coronal count at the continuum region of the spectrum. Then the disk spectrum is subtracted from the coronal spectrum. This process removes the background in the coronal spectrum. All the 501 spectra were analyzed similarly to derive the above-mentioned emission line parameters as a function of time, and spatial locations along the slit. The image shown in Figure 2 was constructed using the peak intensity of the emission line for the spectra due to the fourth slit. The x -axis in the image corresponds to time (12:00–19:00 UT). The y -axis is the solar position angle (θ), measured counterclockwise from north through east. It corresponds to the range $280^{\circ}\text{--}305^{\circ}$ for these observations. Enhanced emission can be seen in the range $\theta \approx 290^{\circ}\text{--}300^{\circ}$ between $\approx 13:50\text{--}16:20$ UT. The maximum intensity of the emission is seen to have shifted upward by $\approx 4^{\circ}$ at $\approx 15:20$ UT. The above angular span of the enhanced emission corresponds closely with the location of the active region AR13721 on the Sun during the same epoch. Its heliographic coordinates are N26W91.² The corresponding $\theta \approx 296^{\circ}$. In view of the active region near the west limb of the solar disk, we decided to keep the fourth slit at the west limb of the occulter edge. Hence, the LSM was positioned as mentioned above. By design, the closest next slit (third slit) is $0.75 R_{\odot}$ to the east of the fourth slit (see previous paragraph). Due to this, the present observations are limited to the fourth slit (see panel (j) image in Figure 3).

Figure 3 shows extreme-ultraviolet 211 Å running difference images of the solar corona near AR13721 on 2024 July 5 at several epochs during 12:29:35–16:29:47 UT. The images were

¹ https://linelists.chiantidatabase.org/ch_line_list_v11.0_2000_10000.pdf

² <https://www.solarmonitor.org/?date=20240705>

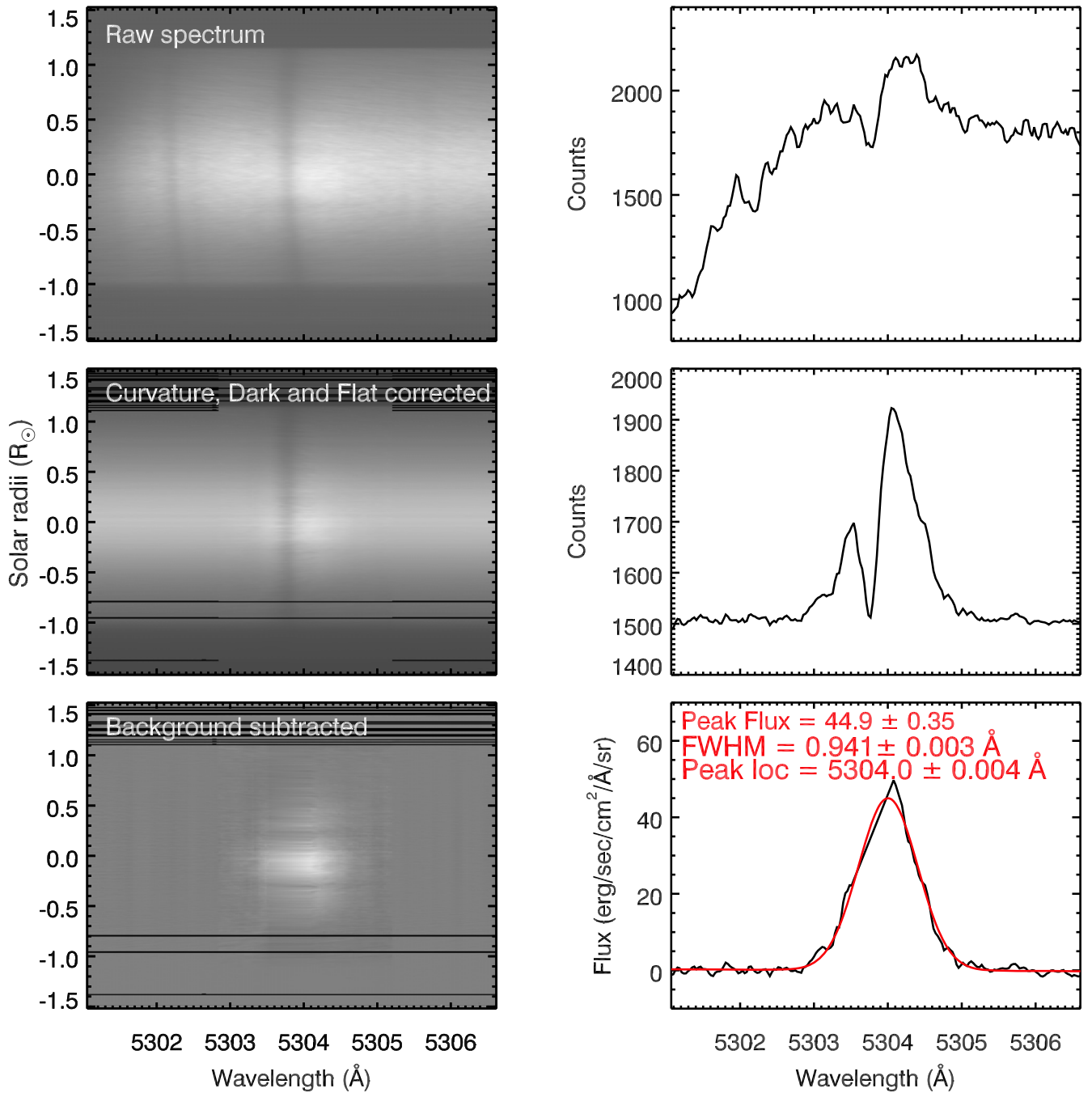


Figure 1. Left panel: The upper image is the instantaneous raw spectrum generated using data obtained with the fourth slit on 2024 July 5. The exposure time is 5 s. Y-axis is the spatial direction along the slit. The spectral dispersion is along the X-axis. The middle image is the spectrum obtained after corrections for curvature, and detector response (dark current & flat-fielding). The lower image is 5303 Å coronal spectrum, after subtraction of the background using the nearly flat region at the center of the filter transmission curve at each spatial location along the slit. Right panel: spectral profiles corresponding to the center of the slit in the respective left panel images. The red color profile is the Gaussian fit to the observed emission line profile after the abovementioned corrections. The observed detector counts were converted into flux units as mentioned in the main text.

obtained with the Atmospheric Imaging Assembly (AIA; J. R. Lemen et al. 2012) on board the Solar Dynamics Observatory (SDO). The box in each panel encloses AR13721. The corona inside the boxed region, as well as outside, appears “quiet” at $\approx 12:29:35$ UT (panel (a)). The image in panel (b) at $\approx 12:59:23$ UT shows faint intensity enhancement within the boxed region. The enhancement indicates a localized increase in the intensity as compared to the intensity in the same area in the previous image. The subsequent images in panels (c)–(f) during the period $\approx 13:29:59$ – $14:59:23$ UT show an increase in

the intensity of the enhancement. The images in panels (g) and (h) at $\approx 15:28:59$ UT and $15:59:23$ UT, respectively, reveal intensity reduction also inside the boxed region, in addition to the intensity enhancement. The regions of enhanced and reduced intensities are located adjacent to each other. The reduced intensity indicates that the emission is lesser in the corresponding localized area compared to the emission in the same area in the previous image. Between the two images in panels (g) and (h), the intensity reduction is comparatively more pronounced in panel (h). This larger reduction implies

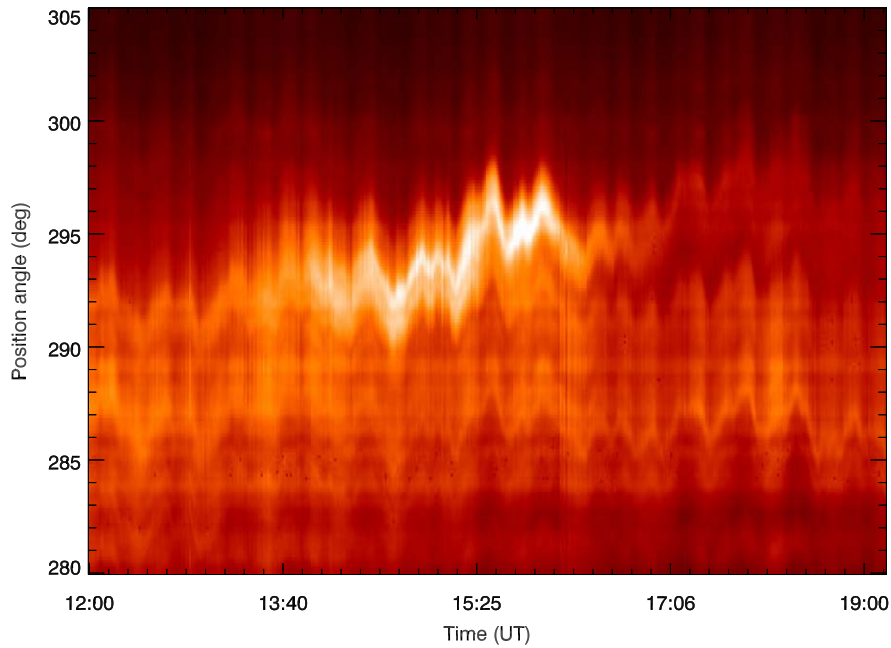


Figure 2. Brightness of the 5303 Å emission line from the solar corona observed along the slit as a function of time on 2024 July 5 with VELC. The enhanced emission in the position angle range $\approx 290^{\circ}$ – 300° is discussed in the main text.

that the intensity of the emission has decreased more. In the panel (i) image at $\approx 16:29:47$ UT, only the dimming is seen. There is also an upward shift ($\approx 2^{\circ}$) in the position of the maximum intensity in the panel (g) image at $\approx 15:28:23$ UT as compared to the panel (e) image at $\approx 14:29:35$ UT. We calculated the above value from the difference between the angles of the respective positions w.r.t the left corner of the box in the two images. Interestingly, a similar shift is seen in the position angle of the enhanced 5303 Å emission in Figure 2 also, at $\approx 15:20$ UT (see previous paragraph).

The upper panel in Figure 4 shows the variation in the flux of the 5303 Å emission line brightness as a function of time, averaged over the position angle range $\approx 290^{\circ}$ – 300° (Figure 2). Enhanced emission could be seen during $\approx 13:00$ – $17:00$ UT, with a maximum between $\approx 15:15$ – $16:00$ UT. The duration between the onset of the enhanced emission and the time at which it reached the maximum is ≈ 2 h15m. The corresponding duration for the decrease to the pre-enhancement level is significantly lesser, ≈ 60 m (i.e., $\approx 17:00$ – $16:00$ UT). The enhancement in intensity during the maximum phase is $\approx 57\%$ [i.e., $(550-350)/350$]. Note that the average heliocentric distance of the coronal regions between position angles 290° and 300° is $r \approx 1.18 R_{\odot}$ as compared to $r = 1.08 R_{\odot}$ for the center of the fourth slit of the spectrograph (see Table 1). This difference is due to the straight nature of the slit. The onset of the enhanced emission at $\approx 13:00$ UT and the decrease in its intensity at $\approx 16:00$ UT show close temporal association with similar signatures in the SDO/AIA 211 Å observations, respectively (see images in panels (b) and (h) of Figure 3). Note the extended phase of the maximum intensity (i.e., $\approx 15:15$ – $16:00$ UT) in the 5303 Å emission although there is an intensity reduction in the SDO/AIA 211 Å images even at $\approx 15:28:59$ UT is likely because there is also enhanced emission in the adjoining region within the boxed area at the same time (see, e.g., panel (g) of Figure 3). The middle panel in Figure 4 shows the variations in the 5303 Å emission line width with time, after correcting for the instrumental line profile. The

widths before and after the intensity enhancement are nearly equal, i.e., 0.97 ± 0.01 Å. It is minimum i.e., 0.87 ± 0.01 Å at $\approx 15:15$ UT. The change in line width is $\approx 10\%$ [i.e., $(0.97-0.87)/0.97$]. The period between the onset of the decrease in the line width and the epoch when it reached the above minimum value is ≈ 2 h15m (i.e., $\approx 15:15$ – $13:00$ UT). This time difference is the same as the duration of the intensity increase mentioned above. The period during which the line width started increasing and again reached the initial level is ≈ 2 h30m (i.e., $\approx 17:45$ – $15:15$ UT). This time duration is longer than the period (≈ 60 m) during which the intensity enhancement decreased from its maximum value to the pre-enhancement level. The lower panel in Figure 4 shows similar variations in the Doppler velocity ($\frac{\Delta\lambda}{\lambda}c$) of the coronal plasma. Here, λ is the rest wavelength of the emission line. The Doppler velocity shows an increasing blueshift and then a decreasing blueshift during the same period as similar variations in the line width. The corresponding amplitudes increased from 0 ± 0.5 km s $^{-1}$ to 3 ± 0.5 km s $^{-1}$ and then decreased back to 0 ± 0.5 km s $^{-1}$. The uncertainties shown in the emission line parameters in Figure 4 were estimated by considering the photometric errors in the observed raw data before any corrections, errors in the dark and flat data, and errors in the Gaussian fit for the emission line. The photometric errors are in the range of 40–60 counts. The rms values of the variations in the dark and flat are ≈ 3.8 and 6.5 counts, respectively. The error in the estimation of emission line intensity from the Gaussian fit is in the range of 10–20 counts. The error bar on each data point in Figure 4 shows the combined error in the derived emission line parameters. The variations in the error during the observing period are in the range $\pm(1.5-2.5)$ erg s $^{-1}$ cm $^{-2}$ Å $^{-1}$ sr $^{-1}$ for the flux, $\pm(0.005-0.01)$ Å for the FWHM, and $\pm(0.1-0.5)$ km s $^{-1}$ for the Doppler velocity. It can be seen that there is an oscillatory pattern in the emission line intensity, width, and Doppler velocity plots in Figure 4. The brightness of the emission line along the slit also shows similar changes (Figure 2). The

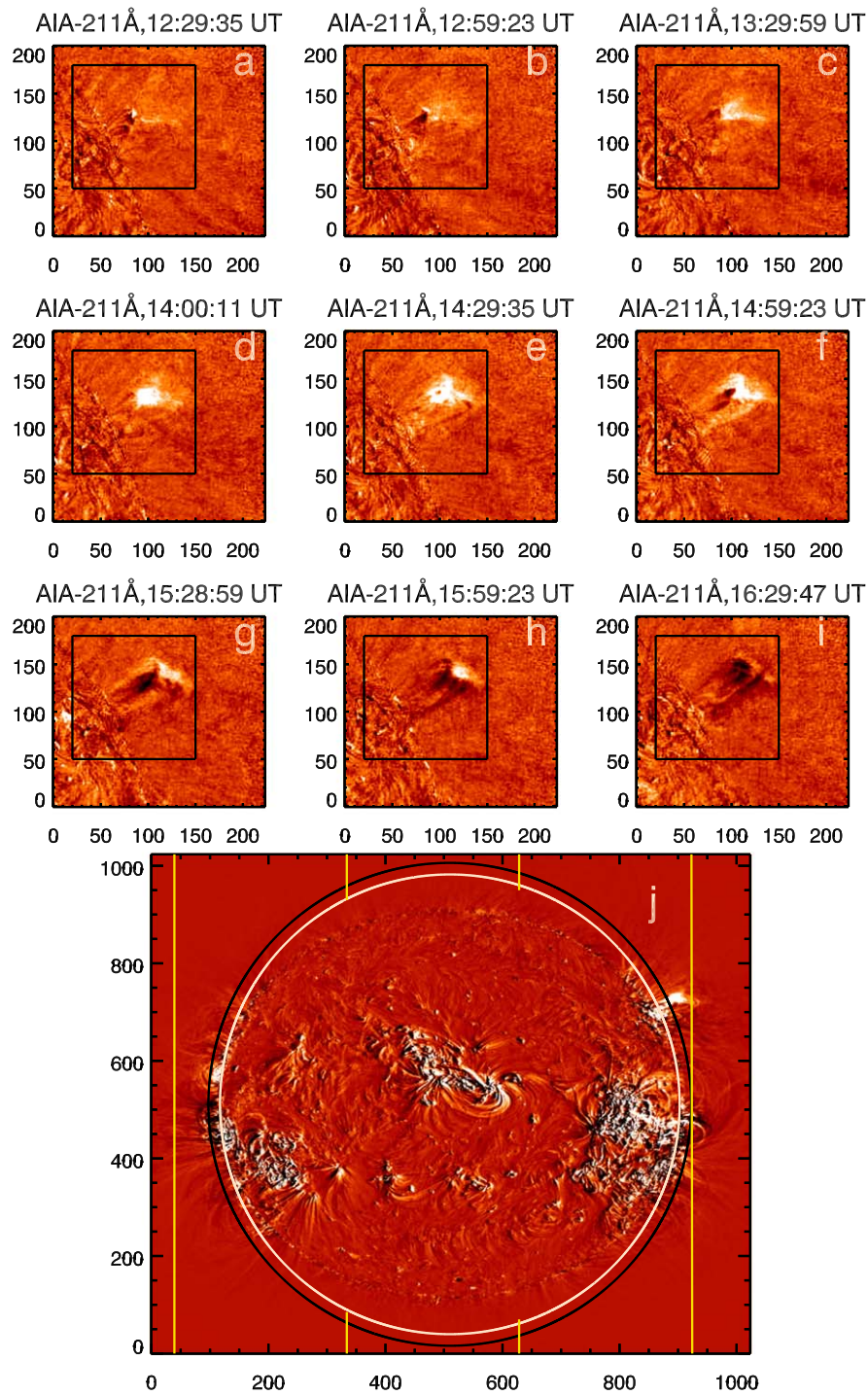


Figure 3. SDO/AIA 211 Å running difference images of the solar corona on 2024 July 5. Solar north is straight up and east is the left. The observing times of the images are mentioned above each panel. The box in each panel encloses the sunspot region AR13721. The image in panel (j) is the full disk version of the partial image in panel (e). The vertical yellow lines indicate the four slits in the VELC spectral channel. The locations of different regions of the solar image w.r.t the four slits, for the VELC observations reported, can be inferred from this image. The white & black circles represent the solar limb and VELC occulter edge, respectively.

amplitude of the oscillations is larger than the uncertainties mentioned above. Assuming that the oscillations are due to changes in the pointing of the spacecraft, we attempted correction using telemetry data on the spacecraft's position and orientation (i.e., SPICE kernels). The data indicated a pointing stability of $\pm 5''$. This corresponds to ± 0.28 change in the position angle (Figure 2). The observed variations are comparatively larger for any effective correction using the SPICE data. We also tried spatial averaging of the data along

the slit. This method too was unsuccessful, probably because the oscillations are there along the entire slit length (Figure 2). Furthermore, the averaging reduced the amplitude of the flux enhancement since the emission is not uniform along the slit. As seen in Figure 4, the period of the oscillations is much shorter compared to the time period of the overall decrease/increase in the emission line parameters due to the evolution of the CME. So, we assume that any effects of the oscillations are expected to be minimal.

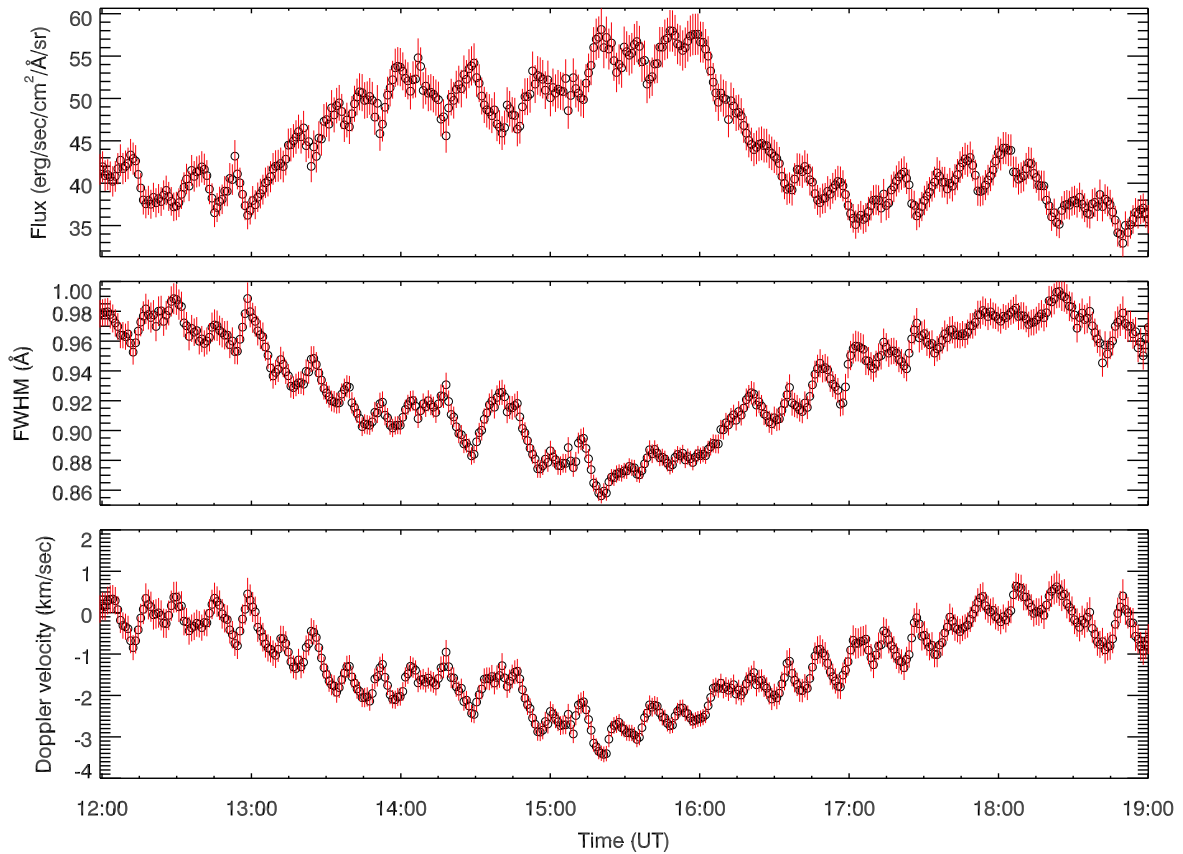


Figure 4. The upper panel shows the time variation of the emission line flux, spatially averaged over the region of enhanced emission in Figure 2 (position angle range $\approx 290^\circ$ – 300°). The middle and lower panels show the corresponding variations in the width and Doppler velocity of the emission line, respectively. The negative (positive) values in the lower panel indicate blueshift (redshift) in the Doppler velocity. The vertical extent of the line on each data point indicates the magnitude of the uncertainties in the estimates.

3. Results and Discussions

The enhanced 5303 Å emission in Figure 2 is observed in the corona at $r \approx 1.18 R_\odot$ as mentioned in Section 2. Our interest is to find out whether it could be due to the passage of a CME across the slit in the spectral channel of the VELC (see, e.g., R. Patel et al. 2021.) Figure 5 shows the white light running difference images of the solar corona available in the Solar Eruptive Event Detection System³ CME catalog generated using observations with the Large Angle Spectroscopic Coronagraph C2 (LASCO-C2; G. E. Brueckner et al. 1995) on board the Solar and Heliospheric Observatory on 2024 July 5 during the period $\approx 14:48$ – $15:36$ UT. The blue arc in all four images indicates the leading edge of a CME, located at $r \approx 4.9 R_\odot$ in the $\approx 14:48$ UT image. The red arc is the approximate outline of the leading edge. The arcs are part of the CME images in the catalog. They are generated in an automated manner from the location (r) of the maximum brightness in the running difference images and their extent in position angle as described in O. Olmedo et al. (2008). The leading edge was near $r \approx 3.4 R_\odot$ at $\approx 12:36$ UT. Compared to this, the start time of the temporal changes in the 5303 Å emission line parameters in Figure 4 at $r \approx 1.18 R_\odot$ is $\approx 13:00$ UT. So, any possible association between the above-mentioned CME (henceforth referred to as the first CME) and the 5303 Å observations in Figure 4 can be ruled out. In

addition to the abovementioned first CME, comparatively brighter emission immediately close to the occulter edge on the west side of the Sun can be seen in the $\approx 15:12$ UT image. It is not there in the previous image at $\approx 14:48$ UT image. The emission is clearly well behind the blue arc (corresponding to the leading edge of the first CME mentioned above) in the $\approx 15:12$ UT image, as well as the subsequent images at $\approx 15:24$ UT and $15:36$ UT. There is no mention of the above emission in the CME catalog. It was probably considered part of the first CME by the automated detection procedure since its position angle is within the angular spread of the first CME. The bright emission has all the attributes of a typical CME, e.g., extended emission brighter than the background and propagating away from the Sun in the coronagraph FoV. So, we assume it to be a CME (henceforth referred to as the second CME). Its leading edge is near $r \approx 2.9 R_\odot$ at $\approx 15:12$ UT. The central position angle and width are $\approx 288^\circ$ and $\approx 36^\circ$, respectively. The estimated linear speed in the plane-of-sky from Figure 4 is $\approx 193 \text{ km s}^{-1}$. The position angles of the active region AR13721 ($\approx 296^\circ$), the enhanced emission in Figure 1 ($\approx 290^\circ$ – 300°), and the second CME described above ($\approx 270^\circ$ – 306°) agree closely. The increase in the line intensity in Figure 3 starts at $\approx 13:00$ UT. SDO-AIA 211 Å images show an increase in the coronal activity at $\approx 12:59$ UT (see image in panel (b) of Figure 2). These two timings are in reasonable agreement with the extrapolated onset time of the CME using the above speed, i.e., $\approx 13:18$ UT at $r = 1 R_\odot$. The above coincidences suggest that the activity in the SDO/AIA 211 Å images in Figure 2, gradual changes in the 5303 Å emission

³ http://spaceweather.gmu.edu/seeds/mkmovie_ql.php?cme=20240705.123607.w057.v0127.p270&frame=20

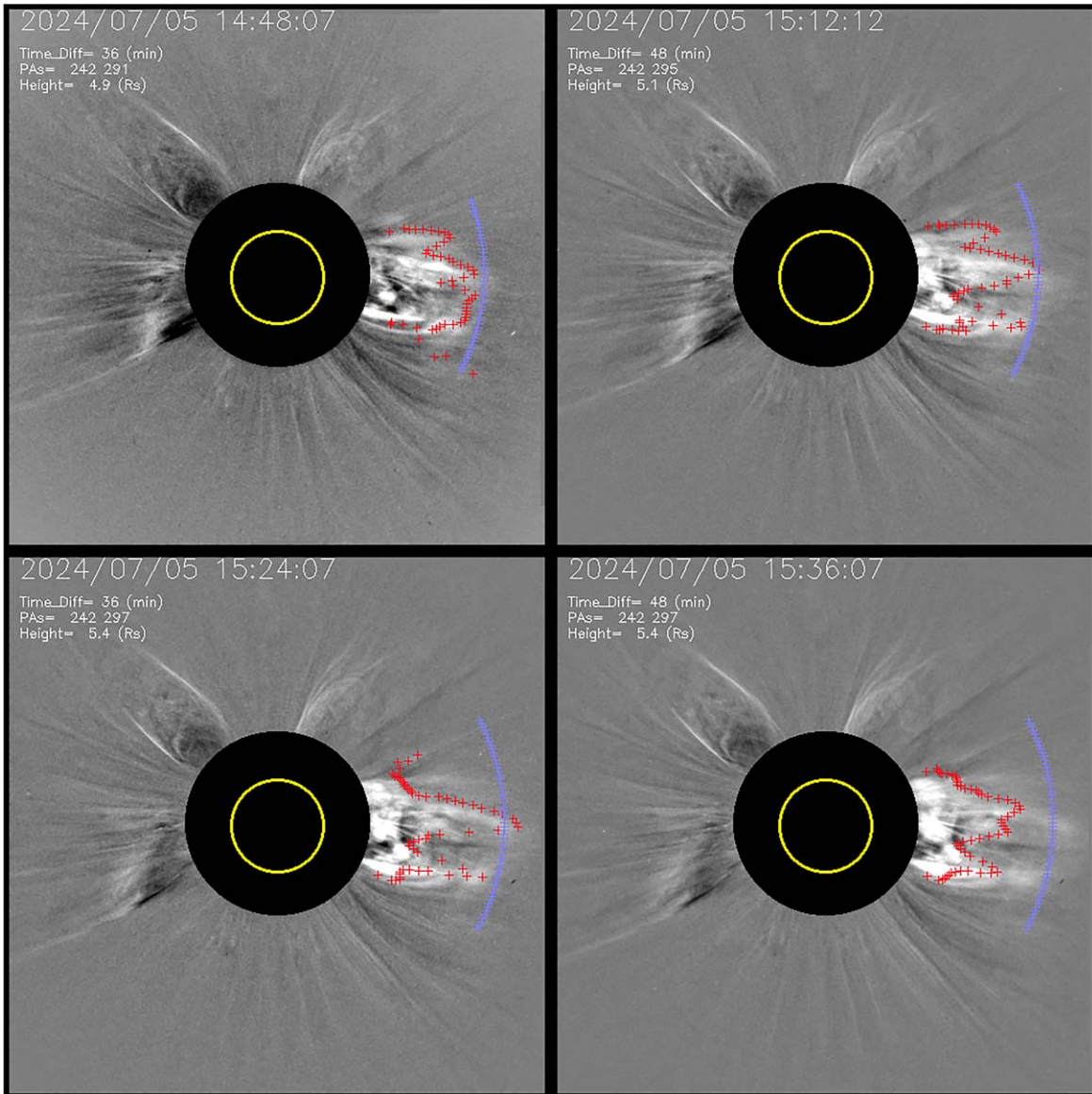


Figure 5. SoHO/LASCO-C2 white light running difference images of the solar corona on 2024 July 5 during the time period in Figures 1, 2, and 3. The observing times of the images are mentioned in each panel. Solar north is straight up and east is to the left. The yellow circle represents the solar limb. The black circle represents the LASCO-C2 occulter. Its radius is $\approx 2.2 R_{\odot}$. The comparatively brighter emission immediately after the occulter on the west (see the images obtained at $\approx 15:12$, $15:24$, and $15:36$ UT) corresponds to the second CME discussed in the main text. The time difference mentioned is w.r.t that of the reference image which was subtracted to generate the images shown. The fainter emission (indicated by the red and blue color arcs) ahead of the abovementioned CME, corresponds to an earlier CME (the first CME in the main text) from the same region. PAs is the position angle range of the first CME as per the red color arc.

line parameters in Figure 3, and the CME in Figure 4 are closely associated. We would also like to add here that the CME was not accompanied by any solar flare.⁴

A closer inspection of Figure 4 shows that the duration of the maximum phase of the line intensity is extended (≈ 45 minutes, starting from $\approx 15:15$ UT) compared to the corresponding phases in both the line width and Doppler velocity, which are limited to a very small duration at $\approx 15:15$ UT. The above-mentioned extended duration of intensity maximum is similar to the results published by R. N. Smartt et al. (1993) from observations of post-flare loops in the 5303 \AA emission line. The authors reported that loop interactions can give rise to enhancements that persist at their maximum for a longer

duration. It is possible that such interactions in the aftermath of the CME onset could be a reason for the extended duration of the intensity maximum in the present case. We pointed out in the previous section that the decrease in the line intensity to the pre-CME level is steeper than the increase in the line width during the corresponding period. The increase in the line width $\approx 15:59:23$ UT in Figure 3 is gradual probably because the SDO/AIA observations show that the intensity enhancement is present even during the intensity reduction as mentioned previously (see, e.g., panel (g) image at $\approx 15:59:23$ UT in Figure 3).

We estimated the effective temperature (T_{eff}) from the emission line width (w) using the relation, $T_{\text{eff}} = \frac{mc^2}{2k_B} \left(\frac{w}{\lambda}\right)^2$. Here $m = 9.33 \times 10^{-26} \text{ kg}$ is the Fe XIV ion mass. Substituting the different values in the above relation, we find that

⁴ https://www.solarmonitor.org/data/2024/07/05/meta/noaa_events_raw_20240705.txt

$T_{\text{eff}} = 3.39 \pm 0.06 \times 10^6$ K before and after the intensity enhancement. It decreased to $2.74 \pm 0.06 \times 10^6$ K during the maximum intensity enhancement. The above values of T_{eff} are in the range of corresponding values reported by Y. Zhu et al. (2024) for the active region corona up to $r \approx 1.6 R_{\odot}$ from their total solar eclipse observations in the 5303 Å line. As mentioned in Section 1, the computed line width and hence T_{eff} have contributions from both thermal and nonthermal components. Therefore, the decrease in T_{eff} can be due to a decrease in either one or both of the above components. Since there were no flares during the observations in the present case, it is possible that there were no changes in the thermal component (H. Zirin 1968). Eclipse observations of the post-CME corona in the 5303 Å emission line indicate that the maximum temperature change close to the Sun is $\approx 5\%$ of the peak formation temperature (B. Boe et al. 2020). Combined observations in white light and 10747 Å emission line indicate that the temperature of the CME plasma remains constant with time in the distance range $r \approx 1.05\text{--}1.35 R_{\odot}$ (J. Sheoran et al. 2023). More recent results reported by C. A. Breu et al. (2024) indicate that any change in the line width due to a change in the thermal component from its peak formation temperature would be very minimal. The observed intensity enhancement in Figure 4 is closely associated with the CME as mentioned in the previous paragraph. It is well known that CMEs are primarily density enhancements above the background coronal-like streamers (see, e.g., C. Kathiravan et al. 2002; R. Ramesh et al. 2021). Hence, the changes in the line intensity in the present case are most likely due to the CME (see, e.g., R. Patel et al. 2021). Assuming $T_i = 1.8 \times 10^6$ K (corresponding to the maximum abundance of Fe XIV ion), we calculated the nonthermal velocities from the line widths. The values are $23.46 \pm 0.5 \text{ km s}^{-1}$ (outside of the intensity enhancement period) and $18.41 \pm 0.5 \text{ km s}^{-1}$ (during maximum intensity enhancement). We would like to note here that recent results based on total solar eclipse observations indicate that $T_i \approx 1.4 \times 10^6$ K at $r \approx 1.2 R_{\odot}$ (B. Boe et al. 2023), nearly the same distance as the enhanced 5303 Å emission reported in the present work (Section 2). If we assume the above value of T_i for our calculations, then the preceding estimates of nonthermal velocities would become slightly higher, $25.86 \pm 0.5 \text{ km s}^{-1}$ and $21.38 \pm 0.5 \text{ km s}^{-1}$, respectively. However, these higher values should be treated with caution. As shown by the above authors, T_i can be higher in regions of turbulent activity. Coronal restructuring, and hence increased turbulence are expected in locations associated with CMEs. Coronal emission in the 5303 Å line is closely associated with CMEs, waves, and turbulence (S. R. Habbal et al. 2021). The line width and hence T_{eff} show a decreasing trend when the line intensity shows an increasing trend and vice versa. The decrease in line width is probably due to a decrease in the amplitude of Alfvénic plasma motions in an increasingly denser plasma and vice versa in an increasingly rarefied plasma (see, e.g., S. McIntosh 2009). Our recent results based on coronal dimming observations in 5303 Å also show an increase in the line width during intensity reduction, and vice versa (R. Ramesh et al. 2024). These imply that the decrease (increase) in the line width with the increase (decrease) in the line intensity in Figure 4 is likely due to CME-associated density changes. It is possible that there was a density increase until the maximum phase of the intensity enhancement. Subsequently, there was a gradual decrease in the density.

The temporal correlations between the intensity enhancement followed by a reduction in the SDO/AIA 211 Å images in Figure 3, and the increase/decrease in the 5303 Å emission line parameters in Figure 4 are in support of this.

The mean Doppler velocity (averaged along the LoS) is $0 \pm 0.5 \text{ km s}^{-1}$ before the beginning of the intensity enhancement, and $3 \pm 0.5 \text{ km s}^{-1}$ during the maximum intensity enhancement at $\approx 15:15$ UT. This gradual increase in the blueshift in the emission is likely due to Earthward side activities in AR13721. In the maximum-end phase of the intensity enhancement, the amplitude of the mean Doppler velocity slowly decreased and reached the initial level, i.e., $0 \pm 0.5 \text{ km s}^{-1}$. The shift in the mean position angle of the enhanced 5303 Å emission (Figure 2) and that of the maximum intensity in the SDO/AIA 211 Å images (Figure 3), both around the same time, probably indicates a change in the direction of propagation of the CME and/or spreading of the activity to the adjacent region, leading to the above decrease in the blueshift. These changes in the position could be due to a deflection by the ambient magnetic field (J. Wang et al. 2020). Similar changes in the activity location and Doppler shift during a CME are mentioned in I. Suzuki et al. (2006).

4. Conclusions

We have reported the first long-duration (≈ 7 hr) temporal observations in the 5303 Å emission line during the occurrence of a CME that was not accompanied by any flare, with VELC. Analysis of the peak intensity of the emission line, as a function of time, indicates a gradual enhancement to a maximum of $\approx 57\%$. Subsequently, the intensity decreased to the pre-CME level. The computed values of the nonthermal velocity decreased from $23.46 \pm 0.5 \text{ km s}^{-1}$ to $18.41 \pm 0.5 \text{ km s}^{-1}$ during the same period as the increase in intensity. Later, the nonthermal velocity increased back to the initial level during the decrease in intensity. Doppler velocity calculations using the locations of the emission line peak during the corresponding period indicate the velocity was $0 \pm 0.5 \text{ km s}^{-1}$ to begin with. Then, its amplitude gradually increased to $3 \pm 0.5 \text{ km s}^{-1}$ (blueshift) around the same time when the line intensity was maximum. Afterward, the amplitude of the Doppler velocity decreased and reached the pre-CME level when the intensity decreased to the pre-CME level. These are interesting and surprising results, hitherto unreported from 5303 Å coronal emission line observations, particularly considering that they are solely due to a CME. B. Boe et al. (2020) had earlier reported similar CME-associated temporal changes in the 5303 Å emission line over a period of ≈ 30 minutes from total solar eclipse observations. Unlike the present observations, it was a “halo” CME and associated with a flare. The above authors noted that the changes were due to the propagation of the CME front which moved plasma of different temperatures along the LoS. The observed changes in the 5303 Å emission line parameters in the present case are likely due to similar effects since the possibility of coronal heating to change the temperature at $r \approx 1.18 R_{\odot}$ is less likely. Combined near-Sun observations with ADITYA-L1/VELC, UCoMP, ASPIICS/PROBA-3, and during total solar eclipses in the future can help to understand the thermodynamic changes in the source regions of the CMEs.

Acknowledgments

We thank P. Savarimuthu and Priya Gavshinde for their assistance in processing the VELC data. The VELC team members who developed the payload are thanked for their efforts. ADITYA-L1 is an observatory class mission that is fully funded and operated by the Indian Space Research Organization (ISRO). Data obtained with the different payloads on board ADITYA-L1 are archived at the Indian Space Science Data Centre (ISSDC). We acknowledge the SDO/AIA and SEEDS teams for providing open data access. We thank the referee for the valuable comments, which helped us to present the results more clearly.

ORCID iDs

V. Muthu Priyal  <https://orcid.org/0000-0001-6093-3302>
 R. Ramesh  <https://orcid.org/0000-0003-2651-0204>
 Jagdev Singh  <https://orcid.org/0000-0003-0562-2979>
 K. Sasikumar Raja  <https://orcid.org/0000-0002-1192-1804>

References

- Altrock, R. C. 2011, *SoPh*, 274, 251
 Boe, B., Downs, C., & Habbal, S. R. 2023, *ApJ*, 951, 55
 Boe, B., Habbal, S. R., Downs, C., & Druckmüller, M. 2022, *ApJ*, 935, 173
 Boe, B., Habbal, S. R., Druckmüller, M., et al. 2020, *ApJ*, 888, 100
 Breu, C. A., Peter, H., Solanki, S. K., Cameron, R., & De Moortel, I. 2024, *MNRAS*, 530, 2361
 Brueckner, G. E., Howard, R. A., Koomen, M. J., et al. 1995, *SoPh*, 162, 357
 Contesse, L., Koutchmy, S., & Viladrich, C. 2004, *AnGeo*, 22, 3055
 Ding, A., & Habbal, S. R. 2017, *ApJ*, 842, L7
 Habbal, S. R., Druckmüller, M., Alzate, N., et al. 2021, *ApJ*, 911, L4
 Habbal, S. R., Druckmüller, M., Morgan, H., et al. 2010, *ApJ*, 719, 1362
 Hara, H., & Ichimoto, K. 1999, *ApJ*, 513, 969
 Hori, K., Ichimoto, K., Sakurai, T., Sano, I., & Nishino, Y. 2005, *ApJ*, 618, 1001
 Kathiravan, C., Ramesh, R., & Subramanian, K. R. 2002, *ApJL*, 567, L93
 Kim, I. S. 2000, in ASP Conf. Ser. 205, Last Total Solar Eclipse of the Millennium, ed. W. Livingston & A. Özgüc (San Francisco, CA: ASP), 69
 Koutchmy, S., Baudin, F., Abdi, S., Golub, L., & Sévre, F. 2019, *A&A*, 632, A86
 Lemen, J. R., Title, A. M., Akin, D. J., et al. 2012, *SoPh*, 275, 17
 Lyot, B. 1932, *ZA*, 5, 73
 McIntosh, S. 2009, *ApJ*, 693, 1306
 Mierla, M., Schwenn, R., Teriaca, L., Stenborg, G., & Podlipnik, B. 2008, *A&A*, 480, 509
 Muro, G. D., Gunn, M., Fearn, S., Fearn, T., & Morgan, H. 2023, *SoPh*, 298, 75
 Olmedo, O., Zhang, J., Wechsler, H., Poland, A., & Borne, K. 2008, *SoPh*, 248, 485
 Patel, R., Megha, A., Shrivastav, A. K., et al. 2021, *FrASS*, 8, 88
 Plunkett, S. P., Brueckner, G. E., Dere, K. P., et al. 1997, *SoPh*, 175, 699
 Prasad, B. R., Suresh Venkata, N., Natarajan, V., et al. 2023, *JATIS*, 9, 044001
 Ramesh, R., Kumari, A., Kathiravan, C., Ketaki, D., & Wang, T. J. 2021, *GeoRL*, 48, e91048
 Ramesh, R., Muthu Priyal, V., Singh, J., et al. 2024, *ApJ*, 976, L6
 Rybanský, M., Rušin, V., Gasper, P., & Altrock, R. C. 1994a, *SoPh*, 152, 487
 Rybanský, M., Rušin, V., Minarovjech, M., & Gasper, P. 1994b, *SoPh*, 152, 153
 Sheoran, J., Pant, V., Patel, R., & Banerjee, D. 2023, *FrASS*, 10, 27
 Singh, J., Ichimoto, K., Imai, H., Sakurai, T., & Takeda, A. 1999, *PASJ*, 51, 269
 Singh, J., Ramesh, R., Prasad, B. R., et al. 2025, arXiv:2503.21184
 Singh, J., Sakurai, T., & Ichimoto, K. 2006, *ApJ*, 639, 51
 Singh, J., Sakurai, T., Ichimoto, K., & Watanabe, T. 2004, *ApJ*, 617, L81
 Smartt, R. N., Zhang, J., & Smutko, M. F. 1993, *SoPh*, 148, 139
 Suzuki, I., Sakurai, T., & Ichimoto, K. 2006, *PASJ*, 58, 165
 Tsubaki, T. 1975, *SoPh*, 43, 147
 Wang, J., Hoeksema, J. T., & Liu, S. 2020, *JGRA*, 125, e27530
 Young, C. A. 1872, *Natur*, 159, 28
 Zhu, Y., Habbal, S. R., Ding, A., et al. 2024, *ApJ*, 966, 122
 Zirin, H. 1968, *ApJ*, 151, 383